Clutter Impacts on Space Based Radar GMTI: A Global Perspective

Ke Yong Li[a], Steven Mangiat[a] , Peter Zulch[b] Unnikrishna Pillai[c],
[a]C&P Technologies Inc., Closter, NJ (201)-768-4448
[b]Air Force Research Laboratory, Sensors Directorate
Rome, NY, (315)330-7861
[c]Polytechnic University, Brooklyn, NY, (718)-260-3732
kli@cptnj.com, steve@cptnj.com, peter.zulch@rl.af.mil, pillai@hora.poly.edu

Abstract—Space based radar has long been considered as a solution to the Department of Defense's requirement for persistent surveillance of the earth surface. Ignoring the logistical issues of launching, deploying, and maintaining a large phased array in space, space based radar has the advantage of being remote and has the capability to perform global surveillance in all weather conditions. [1] [2]

In this paper effects such as earth rotation, range fold over, varied terrain types and internal clutter motion are analyzed for their impacts on space based radar performance. Publicly available data bases allow for the characterization of the entire earths surface in terms of land cover and wind. From this data site specific clutter returns can be generated in a high fidelity radar simulation which can in turn be analyzed to produce performance comparisons under various effects.

More over, a new class of waveforms referred to as '*hybrid chirps*' are introduced that can be used to resolve the range fold over (ambiguous returns) impact seen by a space based radar. These ambiguous range returns, when impacted by earth rotation, can impart delirious effects to minimum discernable velocity performance. The impacts of the afore mentioned effects on minimum discernable velocity, and the benefits of transmit waveform diversity to counter these effects are presented in this paper.

TABLE OF CONTENTS

1. INTRODUCTION

New technologies have evolved for SBR making the concept affordable and suitable for commercial and military applications [1]. Given the affordability of a multiple satellite constellation, the potential exists for day-night, all-weather coverage of the Earth's surface. The resulting capability provides significant possibilities for SBR signal exploitation including Earth surface characterization and military surveillance applications.

This paper will consider the Ground Moving Target Indication (GMTI) mission for a Low Earth Orbit (LEO) altitude Space Based Radar (SBR) with multiple phase centers to enable clutter cancellation for moving target detection. Ground moving target returns must be discriminated from clutter returns based on Doppler frequency. A practical low frequency SBR antenna will present a large mainbeam footprint on the ground with a large clutter Doppler spread, thus masking slow moving targets. Moreover, SBR is susceptible to an Earth Rotation (ER) induced crab angle and magnitude between the platform centerline (or antenna long axis), and its effective platform velocity vector as seen from the ground. This crab angle imposes a range dependent Doppler shift in the clutter returns hence exacerbating the clutter Doppler spectral spread [2][3]. Furthermore range fold over (range ambiguities), contribute to the problem. This increased spectral spread negatively impacts Minimum Discernable Velocity (MDV), thus degrading GMTI performance [4][5][6][7][8][9].

To demonstrate the impacts of ER on SBR a notional L-band LEO SBR system is considered [10]. First, the phenomenology of a SBR and the impacts of ER are introduced. Secondly, wind modeling is introduced which will have an added impact on MDV. Third, MDV performance is analyzed under various ICM conditions for various terrain types from a global perspective. ER and range fold over impacts on MDV are then presented under clairvoyant (known covariance matrices) conditions. And lastly, waveform diversity methods for ER/range fold over impact mitigation are discussed and demonstrated.

2. THE SBR SYSTEM

Historically, airborne surveillance radars have been fielded at low frequencies such as UHF and S-band for Airborne Moving Target Indication (AMTI) and X-band for GMTI. Dual uses for each frequency band include Foliage Penetration (FOPEN) for UHF and imaging for X-band. A

1

[1] 1-4244-0525-4/07/$20.00 ©2007 IEEE.
[2] IEEEAC paper #1082, Version 12, Updated Nov 20, 2007

solid state active array design, employing multiple phase center apertures and adaptive processing is of interest for the purpose of adaptive beamforming and Space Time Adaptive Processing (STAP) interference mitigation.

An L-band LEO system, considered here, has attracted the interest of US Air Force and NASA as a *dual application* sensor [10]. The joint mission focuses on elements of NASA's earth science enterprise strategic plan and the Air Force long term needs for global GMTI and AMTI surveillance, and represents an unprecedented multi-agency approach to scientific and technological advancement of spaceborne radar technology.

Space Based Radar System

Notional parameters for an L-Band LEO-orbit SBR are given in Table 1 and were partially derived from [11]. The array features 16 half overlapped receive subapertures. The full aperture was used for transmit. The 3 dB azimuth X elevation main beam footprint size is approximately 15 km X 800 km.

Table 1. L-Band SBR Parameters

Parameter	Value	Units
Center Frequency	1.25	GHz
Coherent Processing Interval	32	msec
Number of Pulses	16	
Pulse Repetition Interval	2	msec
Compressed Pulse	0.5	μsec
Noise Figure	0	dB
Receiver Ohmic Losses	1.5	dB
Transmitter Ohmic Losses	1.5	dB
Tx Hor. Taper, Taylor	40 (8)	dB
Tx/Rx Vertical Taper	Uniform	
Horizontal Receive Sub-apertures	12	
Rx. Sub-Ap. Hor. Taper, Taylor	20 (8)	dB
Mechanical Az. Steering	90	degrees
Mechancial El. Steering	0	degrees
Radar Altitude	506	km
Radar Speed (inertial velocity)	7,612.7	m/s
Orbit Inclination	90	degrees

Space Based Radar Modeling

Modeling of the system given in Table 1 was done in MATLAB. SBR data generation involves a transmitter-receiver array sending a sequence of pulsed waveforms that excite the various terrains under the field of view. The array gain pattern modulates the transmit waveform and depending upon the terrain-specific radar cross section (RCS), backscattered returns are generated. Ground clutter is modeled as a number of clutter cells, or patches, at an $(i,j)^{th}$ azimuth-range(elevation) location with a backscattered amplitude return $c_{i,j}^{(k)}$ at range bin k.

The returns from the k^{th} range bin are collected over M pulses by an N-element array, with array amplitude factor $A_{i,j}$. These returns for the k^{th} range bin are conveniently combined in a space-time data vector $\boldsymbol{x}_k$ of size $MN \times 1$,

$$\boldsymbol{x}_k = \sum_i \sum_j \frac{c_{i,j}^{(k)}}{R_{s_j}^2} A_{i,j}\, \boldsymbol{s}_{i,j}. \qquad (1)$$

R_{s_j} the slant range, and $\boldsymbol{s}_{i,j}$ represents the associated space-time steering vector. Note that [12]

$$\boldsymbol{s}_{i,j} = \boldsymbol{s}(\boldsymbol{\theta}_{i,j}, \omega_{d_{i,j}}) = \boldsymbol{b}(\omega_{d_{i,j}}) \otimes \boldsymbol{a}(\boldsymbol{\theta}_{i,j}). \qquad (2)$$

where $\boldsymbol{b}(\omega_{d_{i,j}})$ is the temporal steering vector and $\boldsymbol{a}(\boldsymbol{\theta}_{i,j})$ is the spatial steering vector with $\boldsymbol{\theta}_{i,j} = (\theta_{Az_i}, \theta_{El_j})$ corresponding to the azimuth and elevation angles at the $(i,j)^{th}$ patch.

The random ground clutter backscattered return $c_{i,j}$ from the $(i,j)^{th}$ patch is determined from a statistical distribution which are defined for each possible local land cover type. Fig. 1 shows a typical land cover map generated from NASA's Terra Satellite [13]. The earth is divided into 1 km^2 patches, each categorized into one of 16 land cover types such as forest, urban, croplands, etc. In terms of the backscattered signal $c_{i,j}$ from the $(i,j)^{th}$ patch, the mean RCS value $\sigma_{i,j}^o$ can be defined as

$$E\left\{ | c_{i,j} |^2 \right\} = \sigma_{i,j}^o. \qquad (3)$$

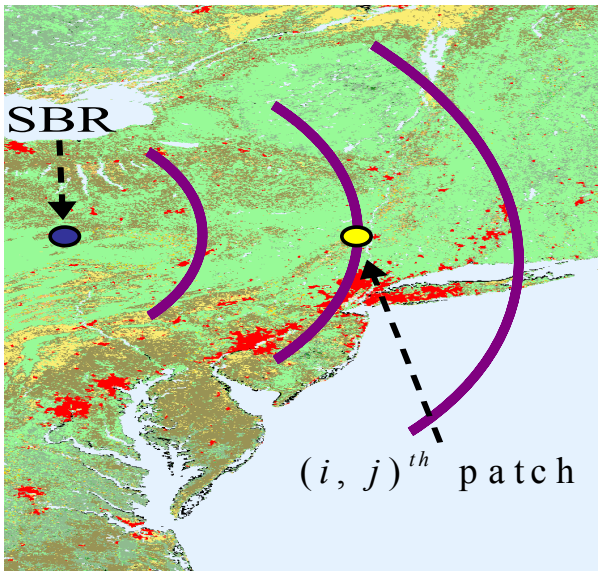

Figure 1 – Land cover map from NASA's Terra Satellite [13].

In general, $\sigma^o_{i,j}$ in (3) depends on the grazing angle. Various models have been proposed to accommodate the grazing angle factor. In the simplest constant gamma model [14], the grazing angle dependency on the mean RCS value is given by

$$\sigma^o(\psi) = \gamma \sin\psi\,, \qquad (4)$$

where γ is a terrain constant and ψ is the grazing angle. This model is found to be reasonable for a large range of grazing angles (10-60°), barring high grazing angles that correspond to near nadir points. At high grazing angle situations, the return power significantly increases. To accommodate this condition, an additional term can be introduced to the constant gamma model in (4). With an extra constant term added to determine the plateau region, the mean RCS takes the form [15],

$$\sigma^o(\psi) = A + B\sin\psi + C\,e^{-D(\frac{\pi}{2}-\psi)^E}\,. \qquad (5)$$

Note that five parameters (A, B, C, D, E) are required to represent this model. Hence, it is often referred to as the "Five Parameter Model". These parameters in turn are determined by the terrain type. Fig. 2 shows the mean RCS $\sigma^o(\psi)$ using the five parameter model for a variety of terrains. Observe that urban has a higher reflectivity, whereas desert (barren) and water have significantly lower reflectivity agreeing with values found in [16].

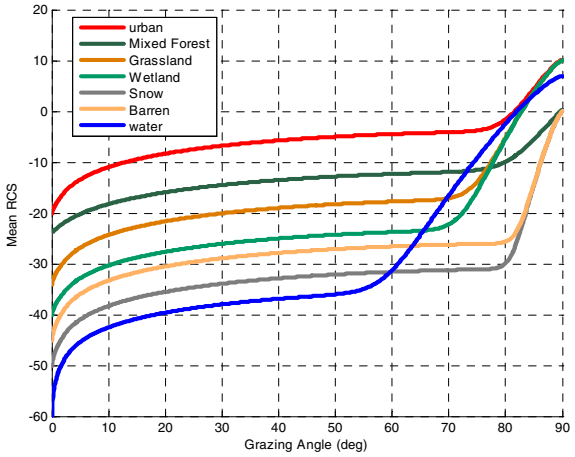

Figure 2 - Five Parameter RCS Model

By fitting various statistical models to experimental data, it has been observed that Weibull distributions effectively model the random amplitude or power levels of the backscattered signal, especially at low grazing angles. Recall that the probability density function of Weibull random variables is given by [17]

$$f_X(x) = \begin{cases} \alpha x^{\beta-1} e^{-\alpha x^\beta/\beta} & x \ge 0 \\ 0 & \text{otherwise.} \end{cases} \qquad (6)$$

Let

$$X = |c_{i,j}|^2\,. \qquad (7)$$

Then, the random backscattered power can be represented as a Weibull random variable whose mean value is given by

$$E\{X\} = \mu_X = \left(\frac{\beta}{\alpha}\right)^{\frac{1}{\beta}} \Gamma(1+1/\beta) = \sigma^o_{i,j}\,, \qquad (8)$$

where the last equality follows from (3) and (7). In (6), β is known as the shape parameter, since $\beta = 1$ gives the exponential distribution and $\beta = 2$ gives the Rayleigh distribution.

In general, knowing the shape parameter β and the mean terrain RCS $\sigma^o_{i,j}$, the other Weibull parameter α in (6) can be computed using (8). For low grazing angles a more accurate mean RCS has been developed as a result of the Phase One study at MIT Lincoln Lab [16]. As the grazing angle decreases the shape parameter β decreases as well, increasing the variance and making the distribution distinctly non-Rayleigh. Fig. 2 together with the Lincoln

Lab low-angle data give an accurate mean RCS for various terrain types, that takes the grazing angle dependency into consideration. In summary, knowing the locations of the SBR and the point of interest on earth, the terrain types, and the mean RCS, the Weibull random variable parameters for the backscattered clutter power can be computed for the entire field of view.

Interestingly, the return amplitude random variable $|c_{i,j}| = \sqrt{X}$ that is useful for simulations is also Weibull-distributed with parameters 2α and 2β. In this paper,, for each location on earth, this procedure is adopted to simulate the backscatter amplitude return random variables $|c_{i,j}|$ for each point in the field of view corresponding to a point of interest with given range and azimuth angle. With a uniform random phase for each $c_{i,j}$, $\boldsymbol{x}_k$ in (1) can be faithfully simulated.

Earth Rotation Doppler Component

For airborne radar the only contributing component to the clutter Doppler frequency is the motion of the platform. For a space platform, operating in inertial space as opposed to earth centered earth fixed coordinate system, the clutter Doppler frequency consists of two velocity components, one due to the platform motion and one due to the earth rotation. These derivations were derived in [6][7] and are briefly repeated here for completeness.

Consider an SBR located at height H above the earth's surface, and for any point of interest D on earth at range R, define the elevation angle θ_{EL} and azimuth angle θ_{AZ} (measured between the SBR velocity vector and the range vector BD) as shown in Fig. 3 and Fig. 4. In that case, the conventional Doppler shift relative to the SBR is given by [18], [19]

$$\omega_d = \frac{2V_p T_r}{\lambda/2} \sin\theta_{EL} \cos\theta_{AZ}, \qquad (9)$$

where T_r represents the pulse repetition rate, λ the operating wavelength and $V_p = \sqrt{GM_e/(R_e + H)}$ the SBR speed. Here, G is the universal gravitational constant and M_e is the mass of earth.

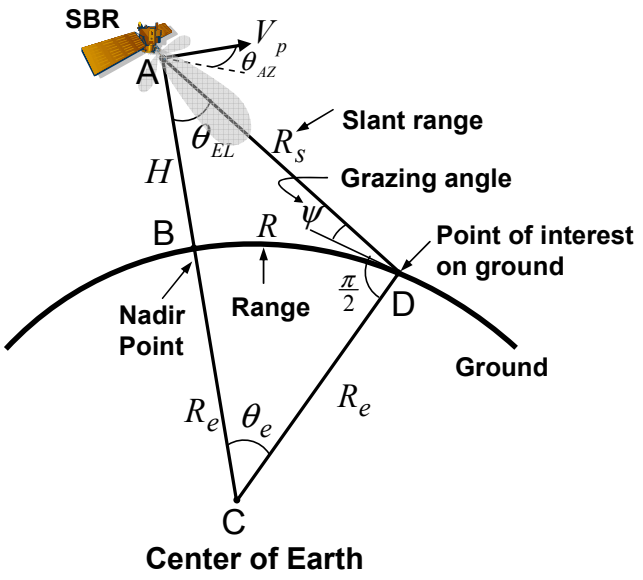

Figure 3 - SBR geometry.

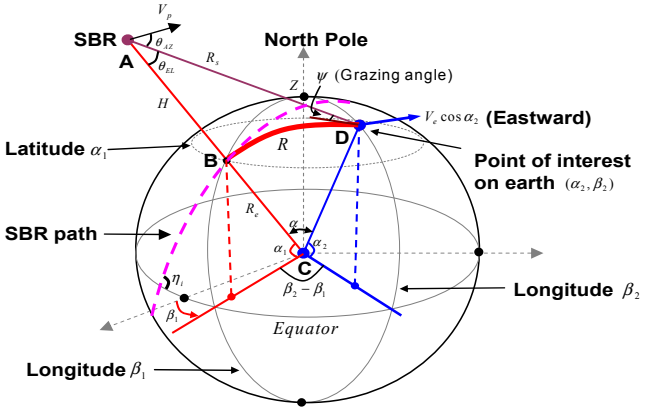

Figure 4 - Doppler contributions from SBR velocity and earth's rotation.

As the SBR moves around the earth, the earth itself is rotating around its own axis on a 23.9345 hour basis. This contributes an eastward motion with equatorial velocity of $V_e = 2\pi R_e/(23.9345 \times 3600) = 0.4651 \text{km/sec}$ that adds an additional Doppler component. After some algebra, the modified Doppler frequency from (9) becomes [9],

$$\omega_d = \frac{2V_p T_r}{\lambda/2} \rho_c \sin\theta_{EL} \cos(\theta_{AZ} + \phi_c), \qquad (10)$$

where

$$\phi_c = \tan^{-1}\left(\frac{\Delta\sqrt{\cos^2\alpha_1 - \cos^2\eta_i}}{1-\Delta\cos\eta_i}\right), \qquad (11)$$

$$\rho_c = \sqrt{1+\Delta^2\cos^2\alpha_1 - 2\Delta\cos\eta_i}\ , \qquad (12)$$

and

$$\Delta = \frac{V_e}{V_p}\left(1+\frac{H}{R_e}\right). \qquad (13)$$

Here α_1 represents the SBR latitude, η_i represent the orbit inclination measured from the equator for the SBR.

In Eqs. (10) – (12), ϕ_c represents the crab angle and ρ_c represents the crab magnitude.

In summary, the effect of earth's rotation on the Doppler frequency is to introduce a crab angle and crab magnitude into the SBR azimuth angle and modify it accordingly. Interestingly both these quantities depend only on the SBR orbit inclination and its latitude and *not* on the latitude/longitude of the clutter patch of interest. Eqs. (10) – (12) correspond to the case where the region of interest D is to the east of the SBR path as shown in Fig. 4. If the region of interest is to the west of the SBR path, the crab angle is the negative (-) of (11).

Figs. 5 and 6 show the crab angle and crab magnitude as a function of the SBR latitude and orbit inclination (η_i) for a SBR at an altitude of 506 km. From Fig. 5 it is seen that the crab angle varies between $\pm 3.7^o$ and has maximum effect for an SBR on a polar orbit located at the equator. The crab magnitude on the other hand has maximum effect when the SBR is on an *equatorial orbit* $(\eta_i = 0,\ \alpha_1 = 0)$. In that case $\rho_c = 1-\Delta$ and leads to about 6% reduction in crab magnitude (refer to Fig. 6). Interestingly, the crab angle has maximum effect on a polar orbit and crab magnitude has maximum effect on an equatorial orbit.

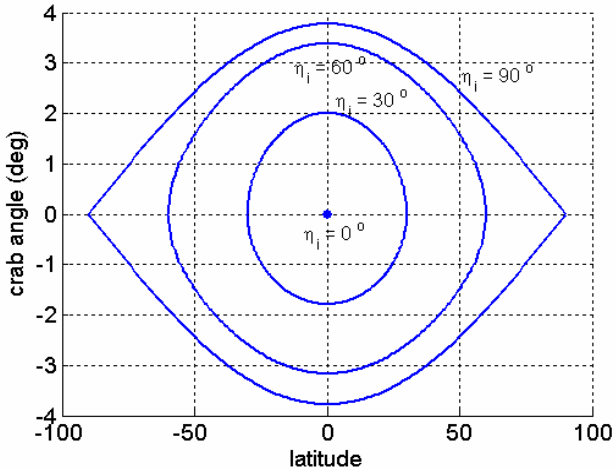

Figure 5 - Crab angle vs. platform latitude for several inclination angles (η_i). Platform at 506 km altitude.

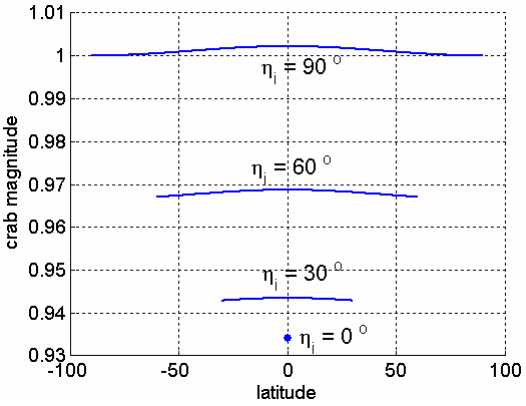

Figure 6 – Crab magnitude vs. platform latitude for several inclination angles (η_i). Platform at 506 km altitude.

Further, irrespective of the inclination angle η_i, the crab angle peaks when the SBR is above the equator. In particular, for an SBR on a polar orbit, the crab angle peaks globally when it is above the equator and its minimum (zero) occurs when it is above the poles.

3. GLOBAL WIND MODELING

Thus far modeling of SBR clutter has been defined based on the geometry and physics of the platform, relationship to the ground scatterer, and earth motion. Another second order characteristic of realistic clutter is Internal Clutter Motion (ICM). This is a problem for space sensors as well as airborne sensors. The primary effect described here comes from forest and water clutter modulations due to the wind.

For the readers interest, Fig. 7 shows the global average monthly wind speed in mph for January and September

[20]. Of special note is the vast difference in wind speed over the ocean areas and slight changes over the land areas.

To model ICM the temporal radar returns are amplitude modulated, thus affecting the Doppler frequency. This means modifying the temporal component in (1) and (2). Consider a uniform pulse sequence with $PRF = 1/T_r$, the temporal steering vector corresponding to *M* pulses has the form [12]

$$\boldsymbol{b}(\omega_d) = \left[1,\ e^{-j\pi\omega_d},\ e^{-j2\pi\omega_d},\ \cdots e^{-j(M-1)\pi\omega_d}\right]^T, \quad (14)$$

where ω_d is given in (9). The wind modulated temporal steering vector has the form [12]

$$\tilde{\boldsymbol{b}}(\omega_d) = \boldsymbol{b}(\omega_d) \odot \mathbf{w}, \quad (15)$$

with

$$\mathbf{w} = \left[w_1,\ w_2,\ \cdots\ w_M\right]^T \quad (16)$$

where $w_1, w_2, \ldots, w_M$ represent the "wind" random variables and $\odot$ is the Schur Product (element-wise multiplication).

Let

$$r_w(kT_r) = E\left\{ w_i\, w_{i+k}^* \right\} \quad (17)$$

be the autocorrelation coefficients of the "wind" random variables in (16).

Billingsley has modeled these windblown autocorrelations as [16],

$$r_w(\tau) = \frac{\mu}{1+\mu} + r(\tau), \quad (18)$$

with the time dependent term $r(\tau)$ given by

$$r(\tau) = \frac{1}{1+\mu}\frac{(c\lambda)^2}{(c\lambda)^2 + (4\pi\tau)^2}. \quad (19)$$

In (18)-(19), μ represents the DC to AC ratio defined by $\mu = 489.8\ v_w^{-1.55} f_0^{-1.21}$, with v_w representing the wind speed in miles/hr, f_0 the carrier frequency in GHz, and

$$c^{-1} = 0.1048\ (\log_{10}(v_w) + 0.4147). \quad (20)$$

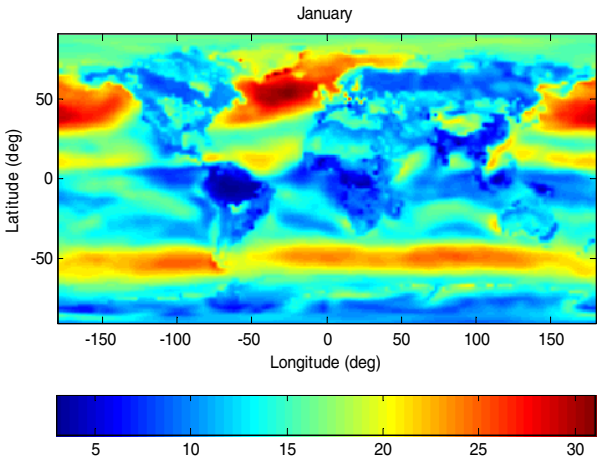

a.)

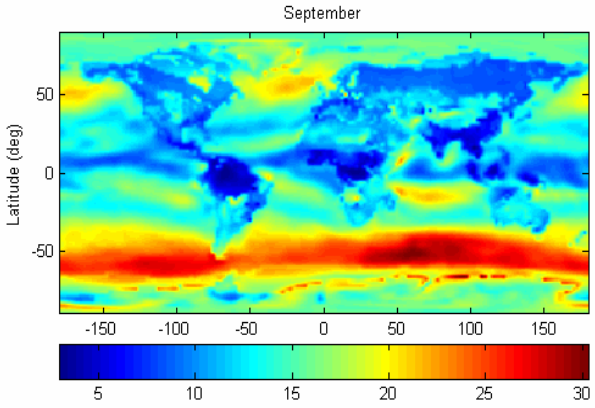

b.)

Figure 7 – Global average wind speeds, a.) January b.) September. [20]

To simulate the windblown random variables in (15)-(16) that satisfy the autocorrelations in (17)-(18), only the time dependent portion $r(\tau)$ in (19) needs to be modeled, and a variety of techniques can be used for this purpose. This discussion is outlined in [21]. The final model for the wind random variables is given as,

$$w_k = -\sum_{i=1}^{m} a_i w_{k-i} + \sum_{i=0}^{m-1} b_i u_{k-i} + c_0 \quad (21)$$

where $\{a_i\}$ and $\{b_i\}$ represent the coefficients of an ARMA filter. Typical values for the coefficients are given in Table 2.

Table 2. ARMA System Coefficients for Billingsley Model, $f_o = 1.25$ GHz, PRF = 500 Hz

Wind (mph)	Order	$a_0 \rightarrow a_m$	$b_0 \rightarrow b_{m-1}$
10	3	1.000000000 -2.917555998 2.839013417 -0.921418618	0.002453600 -0.005191003 0.002887254
30	6	1.000000000 -5.642539629 13.278240033 -16.681541505 11.800863527 -4.457359397 0.702336994	0.004698753 -0.021833017 0.040801158 -0.038280065 0.018015394 -0.003402063
80	6	1.0000000000 -5.522320350 12.723036421 -15.655963091 10.853636468 -4.019910201 0.621520855	0.0074985190 -0.0341922920 0.0629394360 -0.0583378060 0.0272206780 -0.005127624

A comparison of the wind spectrum calculated various ways is shown in Fig. 8. The original spectrum, found by Fourier transforming (18), is given for comparison. The spectrum resulting from sampling and Fourier transforming the autocorrelation function matches very well with the original spectrum. A sixth order rational approximation spectrum is able to faithfully reproduce the wind spectrum up to approximately -60 dB.

4. SBR Performance Analysis

One interest to the SBR user community is the MDV performance predictions of ground moving targets. MDV is typically determined at the output of a clutter nulling filter (or STAP). The radar parameters, environmental conditions, and filtering method all impact this performance. For analysis here the true, or clairvoyant, clutter characteristics are known. With the phenomenology and mathematical models outlined in previous sections, SBR simulations can be carried out to generate data and then in turn this data is processed via STAP and results are analyzed in terms of MDV impact.

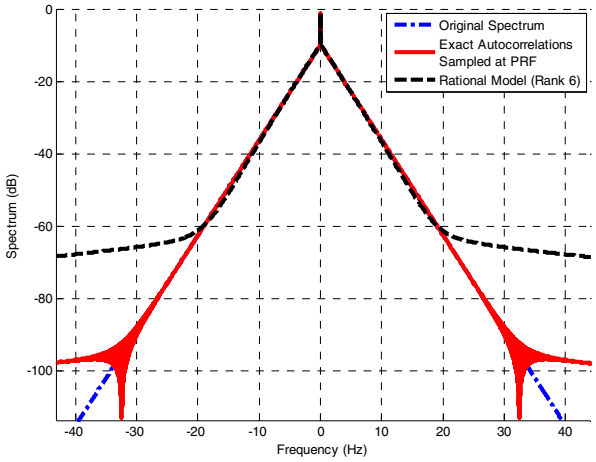

Figure 8 –Wind Spectrum using Billingsley Model, exact autocorrelations sampled at PRF, and sixth order rational approximation. $v_w = 30$ mph, $f_o = 1.25$ GHz, PRF = 500 Hz

Performance Metric

The metric of choice for showing MDV results in Signal to Interference plus Noise Ration (SINR), defined as [12]

$$SINR = \boldsymbol{s}^H(\theta_{i,j}, \omega_{d_{i,j}})\boldsymbol{R}^{-1}\boldsymbol{s}(\theta_{i,j}, \omega_{d_{i,j}}) = \boldsymbol{s}^H\boldsymbol{R}^{-1}\boldsymbol{s}. \quad (22)$$

The superscript H denotes here the complex conjugate transpose operation. where $\boldsymbol{s}(\theta_{i,j}, \omega_{d_{i,j}})$ represents the normalized space-time steering vector as in (2) for the desired *i,j* clutter patch. The clairvoyant covariance matrix for the range cell co-located with the *i,j* clutter patch is denoted as $\boldsymbol{R}$. The ideal clutter covariance matrix for range cell k is

$$\boldsymbol{R}_k = E\left\{\boldsymbol{x}_k \boldsymbol{x}_k^H\right\}, \quad (23)$$

where the $MN \times 1$ clutter data vector $\boldsymbol{x}_k$ is given in (1) and (2). For the ideal case (23) can be written as,

$$\boldsymbol{R}_k = \sum_{i}^{N_o}\sum_{m=0}^{N_a} P_{im} G(\boldsymbol{\theta}_{im}) \boldsymbol{s}_{im}\boldsymbol{s}_{im}^H + \sigma^2 \boldsymbol{I}. \quad (24)$$

Here the inner summation is over the N_a range foldovers at $R_1, R_2, \ldots, R_{N_a}$, and the outer summation is over N_o azimuth angles of interest $\theta_{AZ,i} = \theta_{AZ} + i\Delta\theta, \quad i = \pm 1, \pm 2, \cdots$. Further, P_{im} and

$G(\boldsymbol{\theta}_{im})$ correspond to the clutter power and array gain, respectively. The space time steering vector at the i^{th} azimuth angle and m^{th} range foldover is given as

$$\boldsymbol{s}_{im} = \boldsymbol{s}(c_{im}, \omega_{d_{im}}). \tag{25}$$

The term c_{im} represents the cone angle for the $(i,m)^{th}$ patch given by

$$c_{im} = \sin\theta_{EL_m} \cos\theta_{AZ_i}, \tag{26}$$

and

$$\begin{cases} \omega_{d_{im}} = \beta c_{im}, & \text{w/o earth's rotation,} \\ \tilde{\omega}_{d_{im}} = \beta\rho_c \sin\theta_{EL_m} \cos(\theta_{AZ_i} + \phi_c), & \text{with earth's rotation} \end{cases} \tag{27}$$

depending on whether earth's rotation is absent or present in (24).

Global Wind Impacts

In this portion of the paper non-wind blown and wind blown site specific clutter impacts on SBR performance are presented. These impacts are measured relative to non-wind blown uniform terrain, the ideal case.

To carry out the needed simulations for this study, terrain classification is realized using NASA's Terra satellite with 1-sq km resolution, which uses a 16-type land/water classification scheme. This data is used to characterize ground scatterer returns as outlined in Section 2. To evaluate the change in performance by introducing such a site-specific terrain model as opposed to uniform terrain, radar clutter was simulated at over 6000 points on the land area of the entire world.

As mentioned, the impacts of wind blown clutter are also of interest. To evaluate the combined effect of wind and terrain modeling on performance, ICM was included in the simulation as discussed in Section 3. Average global wind speeds were obtained using readily available global wind maps [20]. An example of such data is shown in Fig. 7.

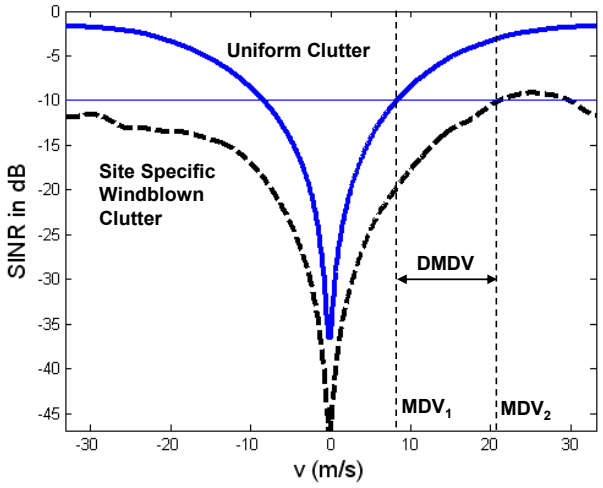

Figure 9 – Description of *Differential MDV,* DMDV.

A differential MDV is defined in order to characterize the relative difference between non-wind blown and wind blown site specific clutter and uniform terrain. Fig. 9 depicts what is meant by *differential MDV*, or DMDV. For purposes here, MDV is defined as the velocity at which the SINR crosses a desired detection threshold [22]. In Fig. 9, at a threshold of -10 dB, MDV_1 represents the MDV using non-wind blown uniform terrain and MDV_2 represents the MDV using the site-specific wind blown terrain (or non-wind blown terrain). Then the DMDV is defined as

$$DMDV = MDV_2 - MDV_1, \tag{28}$$

which represents the degradation/improvement of the site-specific terrain wind blown model (or non-wind blown) vs. uniform terrain for a fixed CNR. Note that due to asymmetry, the MDV represents the average of the positive and negative velocities at which the SINR crosses the desired threshold. If $MDV_2 > MDV_1$, this implies that the more detailed site-specific model here indeed results in inferior performance. It is clear that if the MDV threshold is set to -5 dB in Fig. 10, the SINR would never reach this threshold. In these cases, the MDV is set to the maximum velocity (43.5 m/s) and the DMDV at a -5 dB threshold is therefore $MDV_{\max} - MDV_1 = 22.4$ m/s. All locations with SINR outputs that do not reach the MDV threshold will have this "saturation" value.

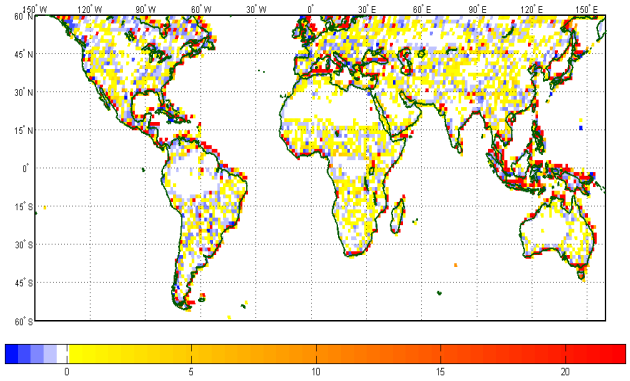

Figure 10 –The global effect of terrain on target detection performance. DMDV is plotted in m/s. Range = 500 km. Azimuth = 90°, CNR = 40dB.

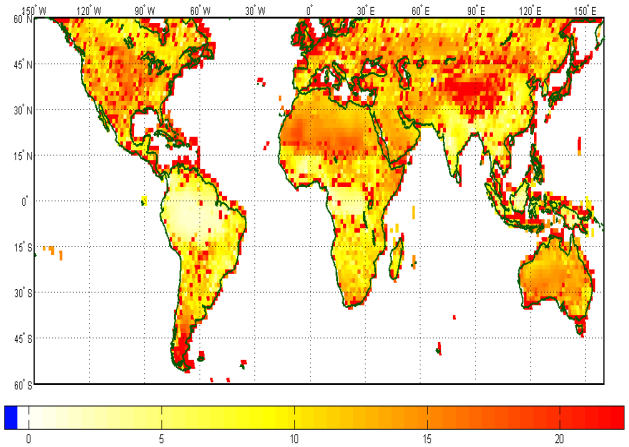

Figure 11 –The global effect of terrain and *wind* on target detection performance. DMDV is plotted in m/s. Range = 500 km. Azimuth = 90°, CNR = 40dB.

Figs. 10 and 11 display the global distribution of DMDV for each of the 6000 locations selected over the land mass of the entire world for the candidate L-band LEO system (MDV threshold is -10 dB). Fig. 10 shows DMDV for site specific terrain *without* wind. Points of interest for this study were chosen if there was land anywhere within 20° of the azimuth look angle. Observe the particularly severe degradation along the coastlines, that occurs because the point of interest is just offshore and nearby land contributes heavily to sidelobe power. The large white areas (corresponding to a DMDV of 0 m/s) cover several of the earth's deserts (such as the Sahara in Northern Africa and the interior of Australia). The terrain type in these areas does not vary, so they are essentially uniform terrain. Fig. 11 shows the DMDV for each location across the globe with site-specific terrain *and* the effect of wind (model from Table 2 used for ICM depends on wind speed). Note the correlation between the strong winds in Fig. 7 and high DMDV in Fig. 11. A more thorough analysis of these findings can be found in [21].

Earth Rotation and Range Fold Over Impact

Now the impacts of earth rotation and range fold over are determined for the candidate L-band LEO SBR under the condition of uniform terrain and clairvoyant covariance matrices. The SBR outlined in Section 2 was simulated and processed with a full dimension Space Time Adaptive Processor (STAP) matched filter and SINR performance was determined. Fig. 12 shows the SINR result as a function of range and Doppler under conditions of no earth rotation or range fold over. The SINR was normalized by the Signal to Noise ratio (SNR) to yield SINR Loss (SINRL). A value of 0 dB for a given Doppler filter represents no loss to signal level, while anything < 0 dB represents a loss due to interference.

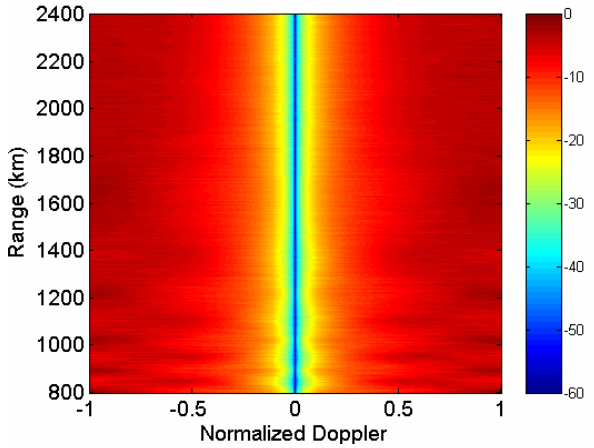

Figure 12 – Matched filter SINRL performance for SBR example, no earth rotation, no range fold over, no wind.

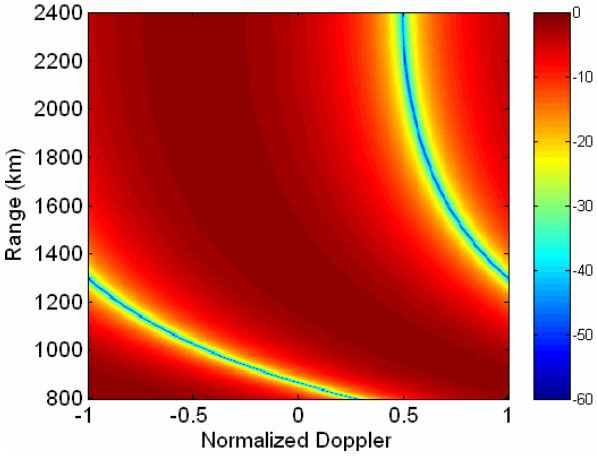

Figure 13 – Matched filter SINRL performance for SBR example, with earth rotation, no range fold over, no wind.

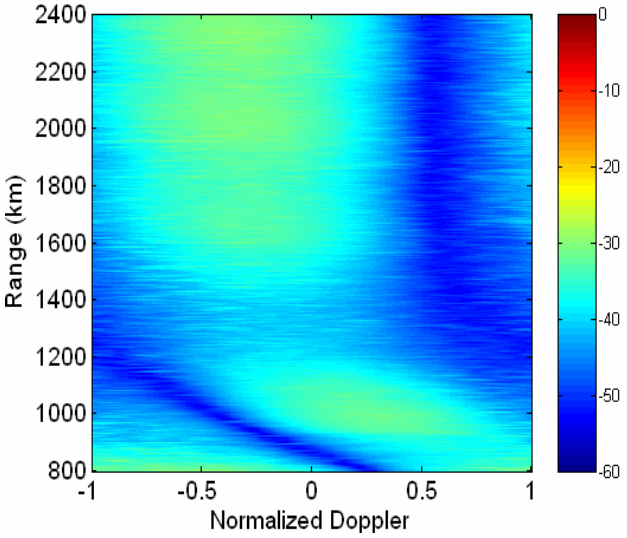

Figure 14 – Matched filter SINRL performance for SBR example, with earth rotation, with range fold over, no wind.

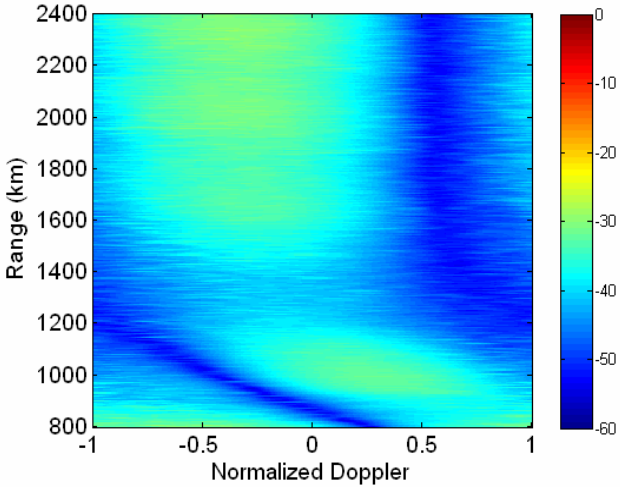

Figure 15 – Matched filter SINRL performance for SBR example, with earth rotation, with range fold over, with 30 mph wind.

Figs. 13 – 15 show the SINRL results for a variety of conditions including earth rotation, range fold over and wind. Note the dramatic range-Doppler profile difference between the cases of without and with earths rotation in Fig. 12 and Fig. 13 respectively. The 'curvature' effect in the earth rotation case is due to the mis-alignment between iso-Doppler contours and iso-conangle contours which is mathematically defined in (27) and discussed in [7][8] and [4].

Obviously one of the most important factors in GMTI performance is usable Doppler spectrum; spectrum that is not inhibited by a high clutter to target ratio, hence obscuring target returns. The range fold over effect clearly exacerbates the problem of earth rotation in terms of usable Doppler space; Fig. 14. Furthermore, ICM also diminishes usable Doppler space as shown in Fig. 15. In this example a 30 mph Billingsley 6th order model was used as parameterized in Table 2.

A further comparison of Figs. 12-15 is done by comparing Doppler profiles for a give range of interest as in Fig. 17. Note that under the condition of range fold over, the earth rotation effect is most dominant effect as compared to ICM.

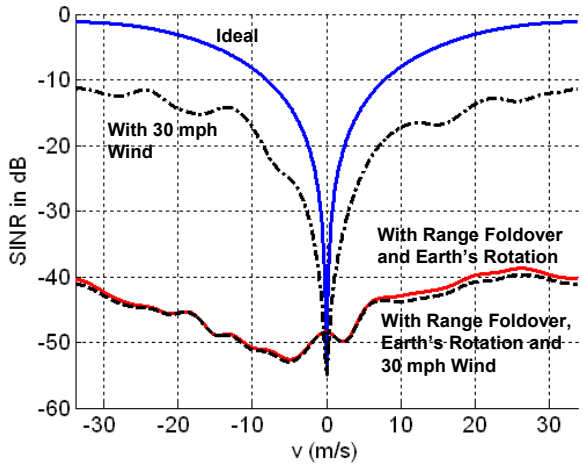

Figure 16 – Comparison of Matched filter SINRL performance for SBR example under various conditions. Ground range = 1,200 km. Ideal corresponds to Fig. 13, ER and fold over corresponds Fig. 14 and ER, fold over, and wind corresponds to Fig. 15.

5. Earth Rotation Mitigation

Earth rotation mitigation methods have been proposed in a number of publications utilizing mechanical antenna steering and transmit waveform diversity [2][3][5][6][23]. Mechanical steering of antenna attempts to correct for the iso-Doppler and iso-cone angle contour misalignment by mechanically steering the antenna to align the long axis of the antenna with the ground track velocity vector [4][5][23]. However it is noted that the mechanical orientation adjustment must change with platform location as the crab angle changes with location as indicated in Fig. 5. This may not be possible due to limitations on power available on the SBR payload. Also this method only corrects for the '*Doppler Warping'* as seen in Figs. 13 and does not resolve the range ambiguities.

Another method suggested to combat the combined effects of earth rotation and range fold over is to change the radar transmit waveform during the coherent processing interval (CPI). A Quadratic Phase Modulation Waveform (QPMW) has been suggested in [2][3] that changes the starting phase of each pulse in order to correct for the *Doppler warp*. This

technique was further analyzed for the LEO L-band system under consideration in [5][23]. This method does an exceptional job of removing the *Doppler warp* hence improving MDV, however at the expense of not resolving the range ambiguities (due to range fold over). The range ambiguous regions are essentially shifted on top of one another in Doppler.

In order to address the combined effect of earth rotation and range fold over, orthogonal waveforms are considered. This was considered for the LEO L-band system in [23]. The goal here was to *code* each range ambiguity with a different orthogonal phase coded sequence. Upon match filtering, the ambiguities (assuming the number of codes equals the number of ambiguities) can be resolved and a range dependent Doppler shift can be applied to remove the remaining Doppler offsets of the different ambiguities due to earth rotation.

In this paper, yet another waveform technique is proposed to realize the goal of minimizing the effects of range fold over. Recall that in ordinary practice, a set of identical pulses are transmitted as in Fig. 17 (a). To suppress the returns due to range fold over, for example, individual pulses $f_1(t)$, $f_2(t)$, $\cdots$, as shown in Fig. 17 (b) can be made orthogonal to each other so that

$$\int_o^{T_o} f_i(t) f_j(t)\, dt = \delta_{i,j}, \quad i,j = 1, 2, \cdots, N_a, \qquad (29)$$

with T_o representing the pulse width and N_a corresponding to the maximum number of distinct range fold overs present in the data. Here $\delta_{i,j}$ is the standard Kronecker delta product. Then, with appropriate matched filtering as shown in Fig. 18, the range ambiguous returns can be minimized from the main return corresponding to the range of interest

The decision instant T satisfies $T \geq T_o$ to maintain (29). In this case, performance will be closer to that shown in Fig. 13. Note that for range fold over elimination, waveform diversity needs to be implemented only over N_a pulses as shown in Fig. 17 (b). For an SBR located at a height of 506 km and an operating $PRF = 500$ Hz, the number of ambiguities $N_a \approx 7$, which includes range from the nadir point to the horizon.

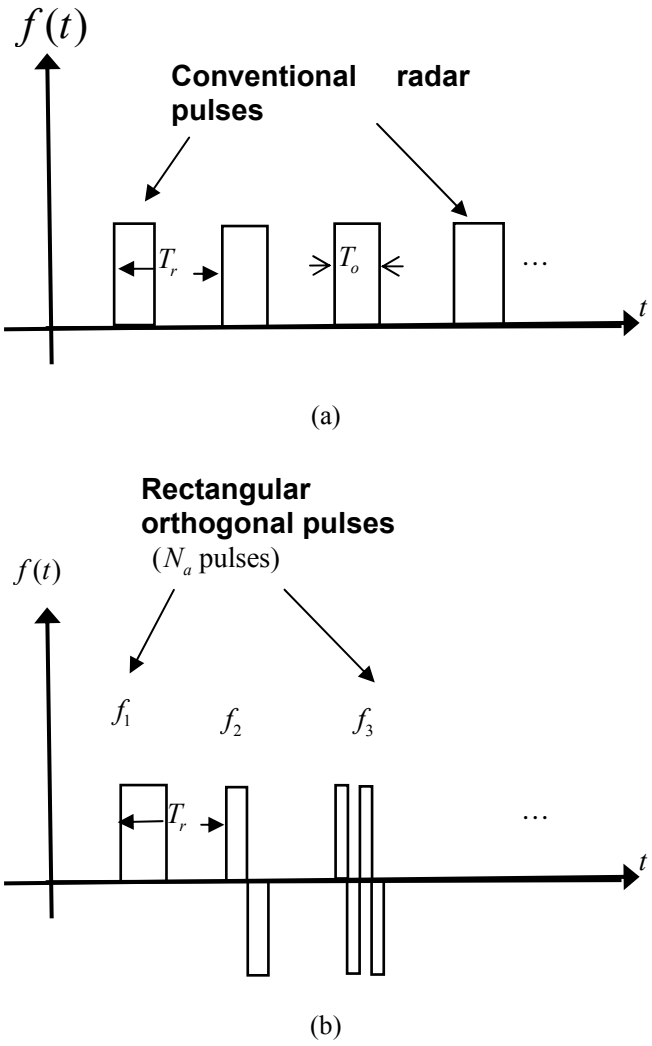

Figure 17 – a) Conventional Radar pulse sequence, b) Radar pulse stream with rectangular pulse waveform diversity.

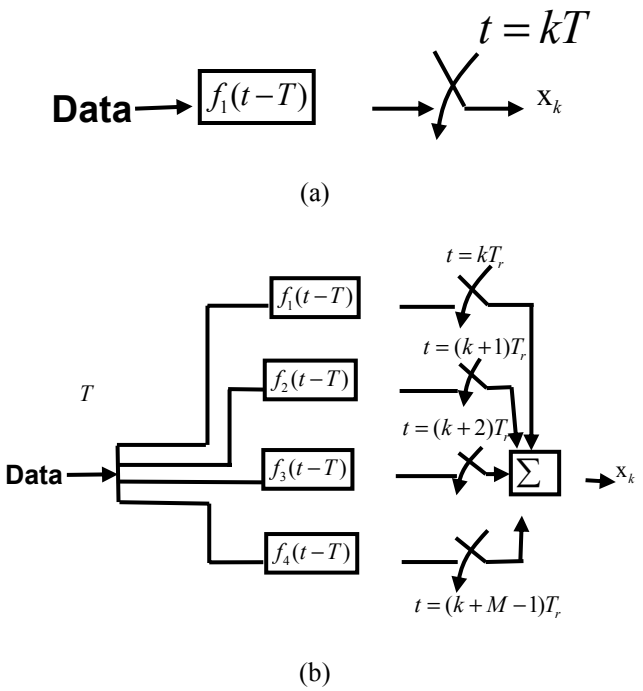

Figure 18 – Match filters, a) without waveform diversity, b) with waveform diversity.

Fig. 19 shows the improvement in *SINR* obtained by using eight rectangular orthogonal pulses as shown in Fig. 17(b). Note that at a ground range of 1200 km, performance is restored since the eight waveforms are able to successfully eliminate the seven range fold over ambiguities present.

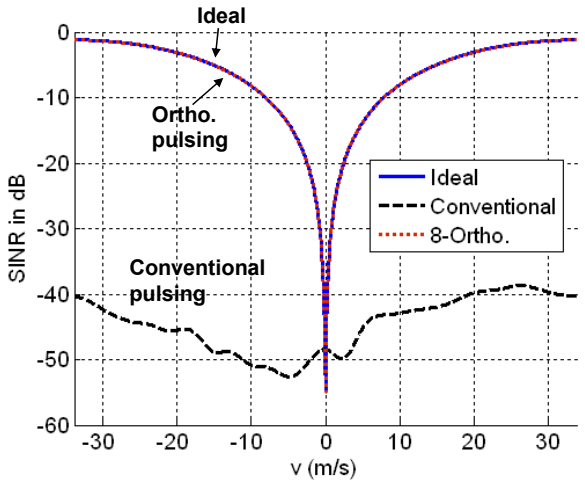

Figure 19 – SINR performance improvement with and without using eight rectangular waveforms at ground range = 1200.

The rectangular pulse waveform scheme in Fig. 17(b) has some practical limitations such as the waveform amplitude not being constant over the CPI; a condition desirable for radar transmitters. A more desirable pulsing scheme is to use pseudo-orthogonal chirp waveforms as shown in Fig. 20. Quadrature phase shifting of these waveforms will generate an additional set of waveforms [9].

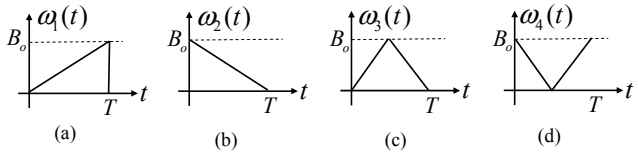

Figure 20 – Up/down chirp waveforms in frequency domain.

Fig. 21 shows the *SINR* improvement using a set of 8 up/down chirp waveforms for the candidate L-band LEO SBR example. Note that these eight waveforms are only approximately orthogonal. In this case, although the performance has improved over the conventional pulsing scheme considerably, the remaining degradation compared to the ideal case can be attributed to the approximate orthogonal nature of these waveforms. A practical set of waveforms that are "more closely orthogonal" should be able to further improve the performance. It will be interesting to determine a set of waveforms with performance that is uniformly close to the ideal case for all ranges of interest (*i.e.*, up to $r_{\max} = 2460$ km for an SBR at a height 506 km).

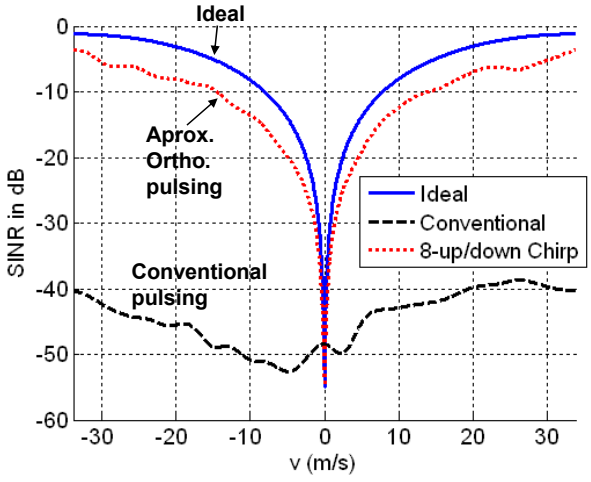

Figure 21 –*SINR* performance improvement *with* and *without orthogonal* pulsing using eight up/down chirp waveforms for ground range = 1200 km.

Fig. 22 shows the improvement in *SINR* as a function of range and Doppler obtained by using these chirp waveforms. For comparison purposes Fig. 23 shows the performance using conventional pulsing when both range fold over and earth's rotation are present. Note that using waveform diversity at transmit, the performance in Fig. 23

is restored to that seen in Fig. 13 where only earth's rotation present.

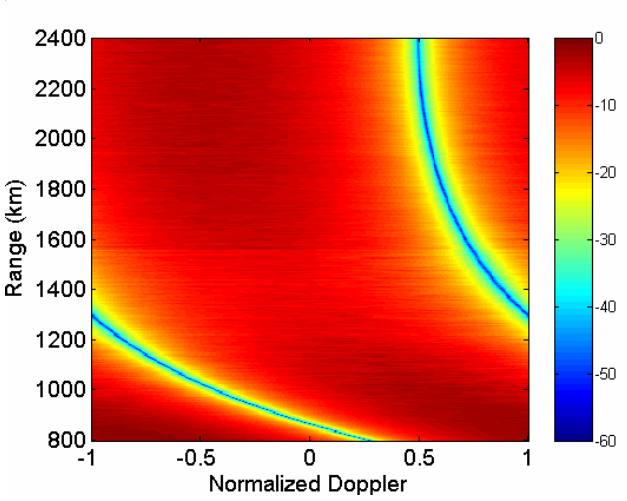

Figure 22 – Matched filter output *SINR* vs. range with range fold over and earth's rotation using eight chirp waveforms that are approximately orthogonal

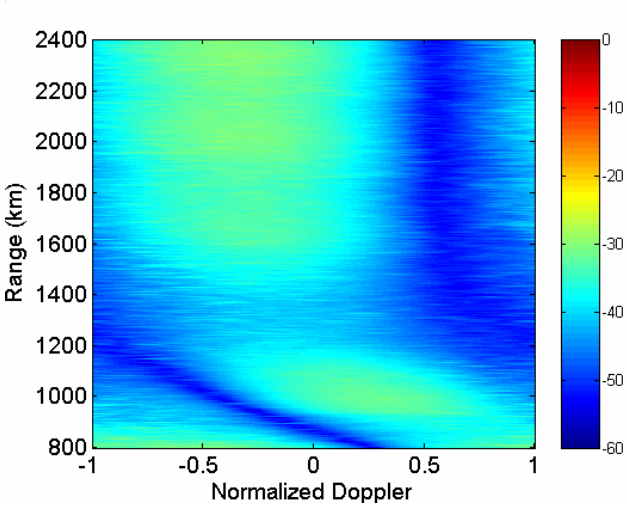

Figure 23 – Matched filter output *SINR* vs. range with range fold over and earth's rotation using conventional pulsing.

6. CONCLUSIONS

Space-borne operation offers many advantages to both the Air Force and commercial users. At the same time it presents many challenges such as the ER impact on MDV presented here. Through simulation studies this paper has introduced the problem and quantified the impact for a candidate L-band LEO SBR system. With some forethought into the orientation of the platform, and/or waveform design, the Earth rotation effect can be mitigated in order to provide a useful system for the Air Force's GMTI mission from space. Waveform diversity has shown to be quite useful in dealing with the ER problem and a new method based on pseudo-orthogonal chirp waveforms has shown promising results. Future plan will be to explore the implementation limitations of such waveforms as well as an optimization process for waveform selection.

REFERENCES

[1] Davis, M.E. "Technology Challenges for Affordable Space Based Radar,'' *Proc. 2000 IEEE International Radar Conference*, pp. 18-23, Alexandria, VA, May 7-12, 2000.

[2] G. A. Andrews, K. Gelrach, "SBR Clutter and Interference", Chapter 11 in Space-Based Radar Handbook, ed. by L. J. Cantafio. Artech House. Boston. 1989.

[3] J.S. Bird and A.W. Bridgewater, "Performance of Space-Based Radar in the Presence of Earth Clutter," *IEE Proc*. Vol. 131, Pt. F, No. 5, pp.491-500. **Need Date!!!**

[4] P. Zulch, M. Davis, L. Adzima, R. Hancock, S. Theis, "The Earth Rotation Effect on a LEO L-Band GMTI SBR and Mitigation Strategies," *Proc. Of the 2004* IEEE Radar Conference, April, 2004.

[5] P.A. Zulch and R.A. Hancock, "Mitigating Earth Rotation Effects on a LEO GMTI SBR," *Proceedings of the 2005 Defense Applications for Signal Processing (DASP),* Midway, Utah, March 2005.

[6] S. U. Pillai, B. Himed, K. Y. Li, "Waveform Diversity for Space Based Radar", Proc. of Waveform Diversity and Design, Edinburgh, Scotland, Nov 8-10, 2004.

[7] S. U. Pillai, B. Himed, K. Y. Li, "Modeling Earth's Rotation for Space Based Radar", Asilomar Conference on Signals, Systems, and Computer, Pacific Grove, CA, Nov 7-10, 2004.

[8] S. U. Pillai, B. Himed, K. Li, "Effect of Earth's Rotation and Range Foldover on Space Based Radar Performance," *Proceedings of the 2005 IEEE International Radar Conference,* Washington DC, 9-12 May 2005.

[9] S.U. Piallai, B. Himed, K. Y. Li, "Effect of Earth's Rotation on Space Based Radar Performance," *Proc. IEEE Transactions on Aerospace and Electronic Systems*, Vol. 42, No. 3, July 2006.

[10]P. Rosen and M. Davis, "A Joint Space-Borne Radar Technology Demonstration Mission for NASA and the Air Force," *Proceedings of the 2003 Aerospace Conference,* Big Sky, MT, March 2003.

[11] M. Davis, J. Maher, R. Hancock, and S. Theis, "High Fidelity Modeling of Space-Based Radar," *Proc. 2003 IEEE Radar Conference*, pp. 185-191, Huntsville, AL, May 2003

[12] J. R. Guerci, Space-Time Adaptive Processing for Radar, Artech House, Boston, 2003.

[13] NASA TERRA Satellite. http://terra.nasa.gov

[14] M, Long, *Radar Reflectivity of Land and Sea*, Artech House. Boston. 2001.

[15] P. Zulch, "Five Parameter Clutter Model", Private Communications, *Air Force Research Lab*, Rome, NY

[16] J. B. Billingsley, *Low-Angle Radar Land Clutter*, William Andrew Publishing. Norwich, NY. 2002.

[17] A. Papoulis, S. U. Pillai, *Probability, Random Variables, and Stochastic Processes*, McGraw-Hill. New York. 2002.

[18] Mark E. Davis and Braham Himed, "L Band Wide Area Surveillance Radar Design Alternatives", *International Radar 2003 – Australia*, September. 2003.

[19] P. Zulch, M. Davis, L. Adzima, R. Hancock, S. Theis, "The Earth Rotation Effect on a LEO L-Band GMTI SBR and Mitigation Strategies," *Proc. Of the 2004* IEEE Radar Conference, April, 2004.

[20] NASA Langley ASDC, "Surface Meteorology and Solar Energy" http://eosweb.larc.nasa.gov/sse/

[21] S. Mangiat, K.Y. Li, S.U. Pillai, and B. Himed, "A Global Perspective on the Effect of Terrain Modeling and Internal Clutter," submitted to *Proc. IEEE Transactions on Aerospace and Electronic Systems*.

[22] Mark E. Davis, Braham Himed, and David Zasada, "Design of Large Space Radar for Multimode Surveillance", IEEE Radar Conference, Huntsville, AL, pp.1-6, May 2003.

[23] P.A. Zulch, R.H. Hancock, W. Moran, S. Suvorova, J. Byrnes, " Transmit Waveform Diversity for Space Based Radar," *Proceedings of the 2006 IEEE Aerospace Conf,* Bigsky, Montanna, March 2006.

BIOGRAPHY

Ke Yong Li was born in GuangDong, China. He received his B.S degree in Electrical Engineering (Summa Cum Laude) from Polytechnic University, Brooklyn, NY in 2003. During 2002 as part of the summer research program, he developed a three-dimensional discreet Wavelet transform for noise removal and motion detection. Since 2003, he has been working at C & P Technologies, Inc., Closter, New Jersey as a staff engineer. His research interests include Space Time Adaptive Processing (STAP), Optimum Trans-Receiver design technology and space based radar signal processing. He has published seven referred conference papers and he is currently pursuing a M.S. degree in Electrical Engineering.

Stephen Mangiat received his B.S degree in Electrical Engineering from Carnegie Mellon University , Pittsburgh, PA in 2005. Since then, he has been working at C & P Technologies, Inc., Closter, New Jersey as a staff engineer. His research interests include Space Time Adaptive Processing (STAP), space based radar (SBR) signal processing and site-specific SBR clutter simulation.

S. Unnikrishna Pillai received his B. Tech degree in Electronics Engineering from the Institute of Technology (BHU), India in 1977, the M. Tech degree in Electrical Engineering from I.I.T. Kanpur, India in 1982, and the Ph.D degree in Systems Engineering from the Moore School of Electrical Engineering, University of Pennsylvania, Philadelphia in 1985.

From 1978 to 1980 he worked as a radar engineer with Bharat Electronics Limited, Bangalore, India. In 1985 he joined the department of Electrical Engineering Polytechnic at University, Brooklyn, New York as an Assistant Professor and since 1995 he has been a Professor of Electrical and Computer Engineering. He is the author of three textbooks: "Array Signal Processing" (1989), "Spectrum Estimation and System Identification" (S. U. Pillai and Theodore I. Shim, 1993), and the fourth edition of "Probability, Random Variables and Stochastic Processes," (Athanasios Papoulis and S. U. Pillai, 2002). His present research activities include spectrum estimation and system identification, waveform diversity, blind identification and Space-Based Radar signal processing.

Peter Zulch received his Bachelors, Masters, and Doctorate from Clarkson University in 1988, 1991, 1994 respectively. From 1994 to the present he has been employed by the Air Force Research Laboratory in two different branches: the RADAR surveillance branch and the RADAR signal processing branch. His interests include multidimensional adaptive signal processing with applications to Airborne

Early Warning RADAR, space based radar, waveform diversity, multi-static radar, and active noise control. Dr. Zulch is a senior member of the IEEE

射 频 和 天 线 设 计 培 训 课 程 推 荐

易迪拓培训(www.edatop.com)由数名来自于研发第一线的资深工程师发起成立，致力并专注于微波、射频、天线设计研发人才的培养；我们于 2006 年整合合并微波 EDA 网(www.mweda.com)，现已发展成为国内最大的微波射频和天线设计人才培养基地，成功推出多套微波射频以及天线设计经典培训课程和 ADS、HFSS 等专业软件使用培训课程，广受客户好评；并先后与人民邮电出版社、电子工业出版社合作出版了多本专业图书，帮助数万名工程师提升了专业技术能力。客户遍布中兴通讯、研通高频、埃威航电、国人通信等多家国内知名公司，以及台湾工业技术研究院、永业科技、全一电子等多家台湾地区企业。

易迪拓培训课程列表：http://www.edatop.com/peixun/rfe/129.html

射频工程师养成培训课程套装

该套装精选了射频专业基础培训课程、射频仿真设计培训课程和射频电路测量培训课程三个类别共 30 门视频培训课程和 3 本图书教材；旨在引领学员全面学习一个射频工程师需要熟悉、理解和掌握的专业知识和研发设计能力。通过套装的学习，能够让学员完全达到和胜任一个合格的射频工程师的要求…

课程网址：http://www.edatop.com/peixun/rfe/110.html

ADS 学习培训课程套装

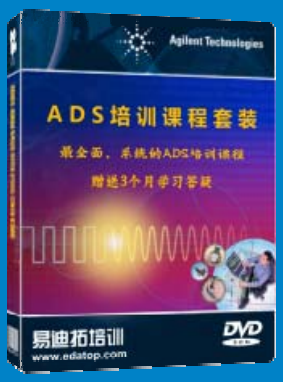

该套装是迄今国内最全面、最权威的 ADS 培训教程，共包含 10 门 ADS 学习培训课程。课程是由具有多年 ADS 使用经验的微波射频与通信系统设计领域资深专家讲解，并多结合设计实例，由浅入深、详细而又全面地讲解了 ADS 在微波射频电路设计、通信系统设计和电磁仿真设计方面的内容。能让您在最短的时间内学会使用 ADS，迅速提升个人技术能力，把 ADS 真正应用到实际研发工作中去，成为 ADS 设计专家...

课程网址： http://www.edatop.com/peixun/ads/13.html

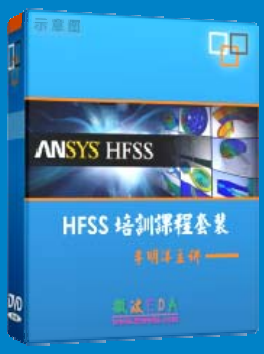

HFSS 学习培训课程套装

该套课程套装包含了本站全部 HFSS 培训课程，是迄今国内最全面、最专业的 HFSS 培训教程套装，可以帮助您从零开始，全面深入学习 HFSS 的各项功能和在多个方面的工程应用。购买套装，更可超值赠送 3 个月免费学习答疑，随时解答您学习过程中遇到的棘手问题，让您的 HFSS 学习更加轻松顺畅…

课程网址：http://www.edatop.com/peixun/hfss/11.html

CST 学习培训课程套装

该培训套装由易迪拓培训联合微波 EDA 网共同推出，是最全面、系统、专业的 CST 微波工作室培训课程套装，所有课程都由经验丰富的专家授课，视频教学，可以帮助您从零开始，全面系统地学习 CST 微波工作的各项功能及其在微波射频、天线设计等领域的设计应用。且购买该套装，还可超值赠送 3 个月免费学习答疑…

课程网址：http://www.edatop.com/peixun/cst/24.html

HFSS 天线设计培训课程套装

套装包含 6 门视频课程和 1 本图书，课程从基础讲起，内容由浅入深，理论介绍和实际操作讲解相结合，全面系统的讲解了 HFSS 天线设计的全过程。是国内最全面、最专业的 HFSS 天线设计课程，可以帮助您快速学习掌握如何使用 HFSS 设计天线，让天线设计不再难…

课程网址：http://www.edatop.com/peixun/hfss/122.html

13.56MHz NFC/RFID 线圈天线设计培训课程套装

套装包含 4 门视频培训课程，培训将 13.56MHz 线圈天线设计原理和仿真设计实践相结合，全面系统地讲解了 13.56MHz 线圈天线的工作原理、设计方法、设计考量以及使用 HFSS 和 CST 仿真分析线圈天线的具体操作，同时还介绍了 13.56MHz 线圈天线匹配电路的设计和调试。通过该套课程的学习，可以帮助您快速学习掌握 13.56MHz 线圈天线及其匹配电路的原理、设计和调试…

详情浏览：http://www.edatop.com/peixun/antenna/116.html

我们的课程优势：

※ 成立于 2004 年，10 多年丰富的行业经验，

※ 一直致力并专注于微波射频和天线设计工程师的培养，更了解该行业对人才的要求

※ 经验丰富的一线资深工程师讲授，结合实际工程案例，直观、实用、易学

联系我们：

※ 易迪拓培训官网：http://www.edatop.com

※ 微波 EDA 网：http://www.mweda.com

※ 官方淘宝店：http://shop36920890.taobao.com